Spacecraft Observations of the Martian Atmosphere*

Michael D. Smith

NASA Goddard Space Flight Center, Greenbelt, Maryland 20771;
email: Michael.D.Smith@nasa.gov

Annu. Rev. Earth Planet. Sci. 2008. 36:191–219

First published online as a Review in Advance on January 2, 2008

The *Annual Review of Earth and Planetary Sciences* is online at earth.annualreviews.org

This article's doi:
10.1146/annurev.earth.36.031207.124334

0084-6597/08/0530-0191$20.00

Key Words

Mars, climate, remote sensing, temperature, dust, clouds

Abstract

Recent spacecraft observations of the Martian atmosphere show that the current climate has a distinct and generally repeatable pattern of seasonal and spatial variations. The half of the year that Mars is closest to the Sun is characterized by warm, dusty conditions, whereas the opposite season is relatively cool, free of dust, and dominated by a low-latitude band of water ice clouds. Water vapor is most abundant at high latitudes in the summertime of both hemispheres, whereas a polar hood of clouds forms over the winter polar region. The greatest year-to-year variations are caused by intermittent large dust storms, which also affect atmospheric temperature and circulation patterns on a global scale.

1. INTRODUCTION

The past decade has seen an explosion in the amount of spacecraft data from Mars. The successful operation of numerous spacecraft at Mars, including the *Pathfinder*, *Mars Global Surveyor* (MGS), *Mars Odyssey*, *Mars Express*, *Mars Exploration Rovers* (MERs), and *Mars Reconnaissance Orbiter* (MRO) have built upon the earlier successes of *Mariner 9* and *Viking* to allow the surface and atmosphere of Mars to be examined in unprecedented detail. There is still much that we do not understand and there are areas that require further observations; however, with the data that is now in hand, it is possible to present a reasonably complete first view of the current Martian climate.

The principal quantities of interest in the characterization of the current Martian atmosphere are surface pressure, atmospheric temperatures, wind velocity, aerosol optical depth and physical characteristics, and the abundance of the gases that make up the atmosphere. All of these quantities can vary with time and location. It is the goal of spacecraft observations to quantify the spatial, diurnal, seasonal, and interannual variations. Once the current atmospheric state has been characterized, the data can then be used with models to understand the physical processes that control the current Martian climate, such as the mechanics of dust storms, the role of clouds, and the interactions between global and local phenomena and between the surface and atmosphere.

Information about atmospheric quantities has been collected in a variety of different ways, which often allows for the validation and cross-calibration between different instruments. From orbit, the primary tools for atmospheric observation have been through thermal infrared sounding, visible imaging of clouds and dust, radio and UV occultations, and near-infrared spectroscopy. From the surface, the primary tools have been imaging of the sky and Sun; thermal infrared sounding; and meteorological packages that typically include sensors for near-surface temperature, atmospheric pressure, and wind velocity. Additional information on atmospheric temperatures and densities has been obtained by accelerometer records during aerobraking passes and the entry, descent, and landing of surface landers.

In this review, we attempt to summarize the current state of the Martian atmosphere below 60 km as observed with spacecraft data. Given the vast amount of data now available, we present just an introduction, not a comprehensive listing of results. We intentionally do not cover ground-based observations of the Martian atmosphere and modeling results. Earlier reviews on spacecraft observations of the Martian atmosphere can be found in the University of Arizona Press book *Mars* (Jakosky & Haberle 1992, James et al. 1992, Kahn et al. 1992, Owen 1992, Zurek et al. 1992) and in papers by Encrenaz (2001), Dlugach et al. (2003), and Liu et al. (2003).

2. THE CURRENT MARTIAN ATMOSPHERE

2.1. Surface Pressure

Surface pressure gives a direct indication of the column-integrated mass of the atmosphere. Surface pressure has been measured by spacecraft using pressure sensors on the *Viking* (Tillman et al. 1993) and *Pathfinder* (Schofield et al. 1997) landers, and

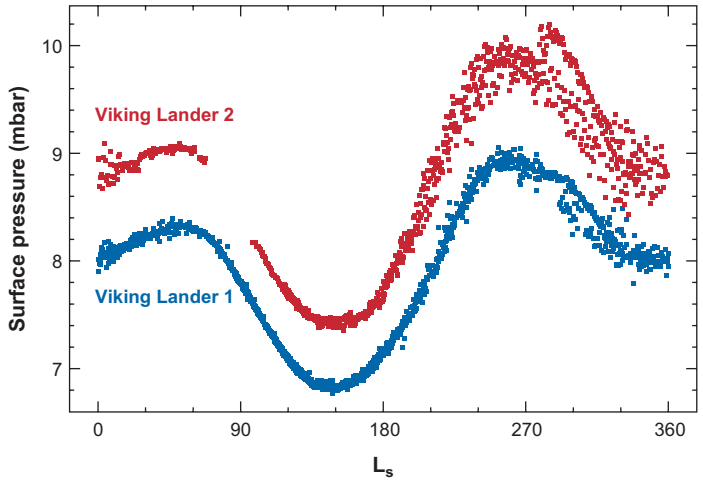

Figure 1

Daily averages of surface pressure (mbar) as recorded by the two *Viking Lander* spacecraft.

by the retrieval of CO_2 column abundance from orbit. Because of their accuracy, frequent sampling, and longevity, the data recorded by the two *Viking Lander* pressure sensors give the most complete picture of the variation of surface pressure at a given location, allowing the study of variations on timescales from hours to interannual.

Figure 1 shows the daily averaged surface pressure recorded by the two *Viking Landers*. The offset between the two curves is caused by the elevation difference (~1.2 km) between the two landing sites. Over the course of a Martian year, surface pressure varies by roughly 30%, decreasing as CO_2 condenses on the seasonal ice cap at the winter pole, and then increasing as CO_2 sublimates from the seasonal ice cap at the summer pole. The timing and differing amplitude of the two annual minima and maxima are caused by the relative phasing of the seasons with respect to the date of perihelion and aphelion in the eccentric orbit of Mars (for more information, see Martian Seasonal Dates sidebar).

In **Figure 1**, the variations superimposed on the annual cycle are the result of traveling waves, similar to the passage of storm systems on Earth (e.g., Leovy 1979). These waves are most prominent in the fall and winter seasons. Diurnal and semidiurnal solar thermal tides cause additional variations in surface pressure on timescales of a day or less. The amplitude of tides has been observed to increase significantly during large dust storms (Zurek 1981).

MARTIAN SEASONAL DATES

Martian seasonal dates are usually given in terms of areocentric longitude, or L_s, which describes the location of Mars in its orbit around the Sun. $L_s = 0°$ is defined as Northern Hemisphere spring equinox (Southern Hemisphere fall equinox), with $L_s = 90°$, 180°, and 270°, following as Northern Hemisphere summer solstice, fall equinox, and winter solstice, respectively.

The near-infrared CO_2 absorption band centered at 2.0 microns is suitable for the retrieval of CO_2 column abundance, and is accessible by the *Mars Express* OMEGA and PFS instruments and the MRO CRISM instrument. Because the atmosphere of Mars is 95% CO_2, the column abundance of CO_2 serves as a reasonable proxy for surface pressure. These orbiters provide spatial sampling of CO_2 column abundance on a global scale, but the temporal sampling at any particular location is not systematic and tends to be at a similar local time.

2.2. Atmospheric Temperature

Atmospheric temperature is one of the most fundamental quantities describing the atmospheric state, and has been inferred using a number of different observational techniques.

2.2.1. Thermal infrared profiling. The most widely used way to infer atmospheric temperatures is through sounding using the thermal infrared 15-micron CO_2 band. The variation in known optical depth as a function of frequency across the band is used to probe atmospheric temperatures at different levels within the atmosphere. Thermal infrared spectra from the *Mariner 9* IRIS (Conrath et al. 1973), MGS Thermal Emission Spectrometer (TES) (Conrath et al. 2000), *Mars Express* Planetary Fourier Spectrometer (PFS) (Grassi et al. 2005a), and MRO Mars Climate Sounder (MCS) instruments have used this approach to retrieve atmospheric temperature profiles. The typical vertical range of sensitivity is from the surface to approximately 40 km with nadir viewing, and as high as 65 km with limb-geometry observations. The typical vertical resolution is approximately one pressure-scale height, or approximately 10 km (Conrath 1972). A single wide-band filter covering the 15-micron CO_2 band on the *Viking Orbiter* Infrared Thermal Mapper (IRTM) (Martin & Kieffer 1979, Wilson & Richardson 2000) and *Mars Odyssey* Thermal Emission Imaging System (THEMIS) (Smith et al. 2003) instruments has allowed a single "average" atmospheric temperature representative of approximately 25 km above the surface to be inferred.

The advantage of thermal infrared profiling is that it allows the retrieval of temperatures over a wide vertical range to be collected systematically on a global scale from an orbiting spacecraft. At present, the best single data set is that obtained by the TES instrument (Smith 2004), which provided near-continuous global coverage of atmospheric temperatures at two different local times (~2:00 AM and ~2:00 PM) on a daily basis for almost three Martian years (March 1999 to August 2004). **Figure 2** shows latitude-height cross sections derived from daytime (~2:00 PM local time) TES spectra for the four seasons, $L_s = 0°$, 90°, 180°, and 270°.

In the cross sections shown in **Figure 2**, temperatures are generally found to depart significantly from radiative equilibrium, indicating strong modifications of the thermal structure by dynamical processes. Under solstice conditions ($L_s = 90°$ and 270°), maximum solar heating occurs at the summer pole, and near-surface temperatures reach a maximum there. In the summer hemisphere, the temperatures at all levels are found to increase toward the pole. In the winter hemisphere, there is a very strong latitudinal temperature gradient between the adiabatically heated local

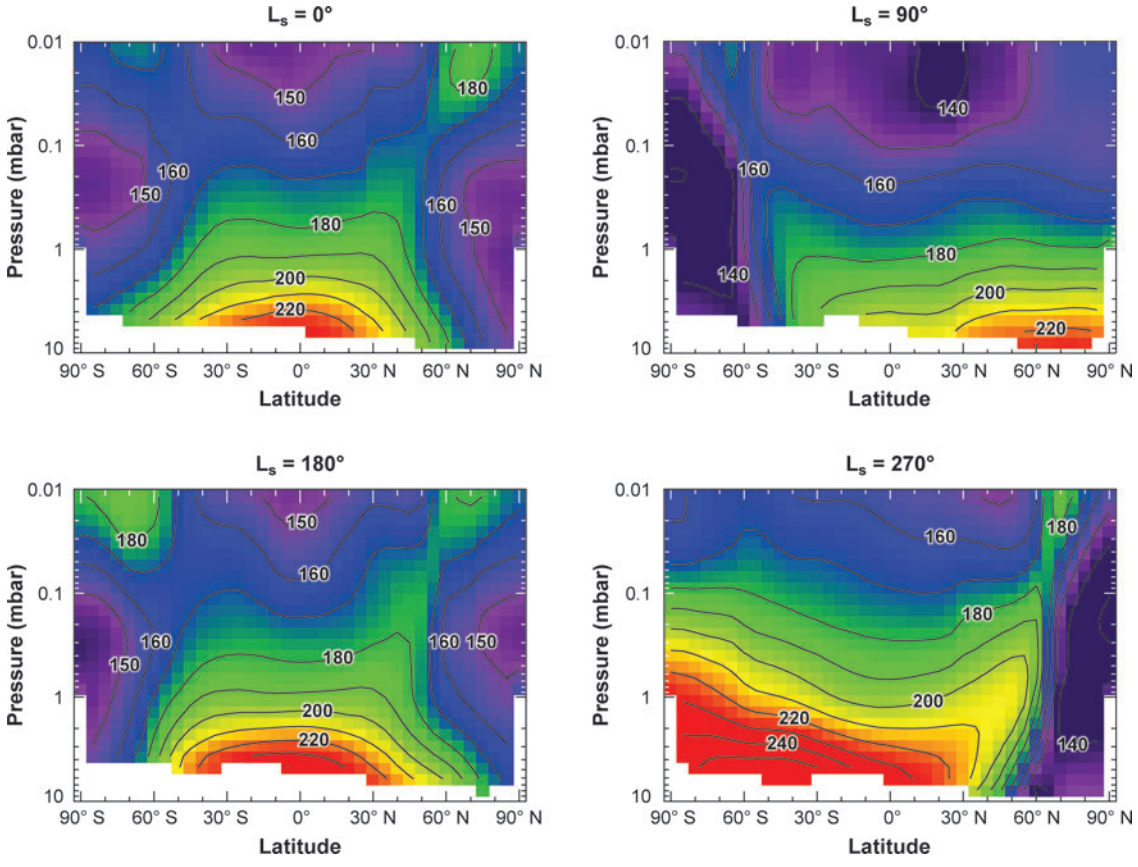

Figure 2

Mean daytime (~2:00 PM local time) temperatures as a function of latitude and pressure (or height above the surface) as observed by TES. The top boundary of 0.01 mbar is approximately 65 km above the surface.

maximum in temperatures caused by downward motions and the very cold temperatures of the polar night. The latitude position of this polar front has a characteristic tilt with the front more poleward at higher altitudes above the surface. This causes a temperature inversion at altitudes below the 1-mbar level at mid-latitudes as cold polar air is advected toward the equator near the surface. The timing of perihelion ($L_s = 251°$) near the Northern Hemisphere winter solstice ($L_s = 270°$) causes a significantly larger latitudinal temperature gradient in winter mid-latitudes in the north than in the south (at $L_s = 90°$). It also leads to warmer temperatures overall during the Southern Hemisphere summer than during the Northern Hemisphere summer.

The thermal structure during the two equinox periods ($L_s = 0°$ and 180°) is similar to each other and is nearly symmetric about the equator. Warmest temperatures are near the surface at the equator. In each hemisphere, temperatures decrease toward the pole at altitudes below ~0.3 mbar (~30 km). Above that pressure level (at least to the

0.01 mbar level), there is a temperature minimum at the equator and a temperature maximum at middle to high latitudes in each hemisphere.

The daily, global-scale monitoring of atmospheric temperatures made possible by TES observations shows a variety of waves, which play an important role in the horizontal and vertical transport of heat, momentum, and atmospheric constituents such as aerosols and water vapor (e.g., Banfield et al. 2003, 2004). Temperature variations are observed that are caused by traveling planetary waves, solar thermal tides, and the interaction of the atmosphere with the large-amplitude Martian topography.

2.2.2. Occultation observations. Radio occultation experiments work by monitoring the signal sent from a spacecraft as it passes behind a planet as viewed from Earth. At both the ingress and egress points, the signal passes through the atmosphere, which both (very slightly) refracts the beam and produces a Doppler shift in the observed frequency. This information can be used to determine the refractive index of the atmosphere as a function of height, which can be converted to temperature given a known atmospheric composition and the assumption of hydrostatic equilibrium.

Radio occultations of Mars have been carried out by the MGS (Hinson et al. 1999). The resulting temperature profiles cover a vertical range from the surface to roughly 45 km, with a vertical resolution of approximately 500 m. The large improvement in vertical resolution over that obtainable using thermal infrared spectra is especially useful for probing near-surface temperatures and for resolving the vertical structure of waves. The disadvantage to the radio occultation temperature profiles is their relatively sparse coverage in space and time, which is limited to the times and places where the spacecraft orbital geometry allows an occultation.

Figure 3 shows selected temperature profiles retrieved from MGS radio occultations. In the afternoon (red profiles), the retrieved temperatures closely agree with the TES results when convolved to the vertical resolution of the thermal infrared profiles (Hinson et al. 2004). At night (blue and purple profiles), the superior vertical

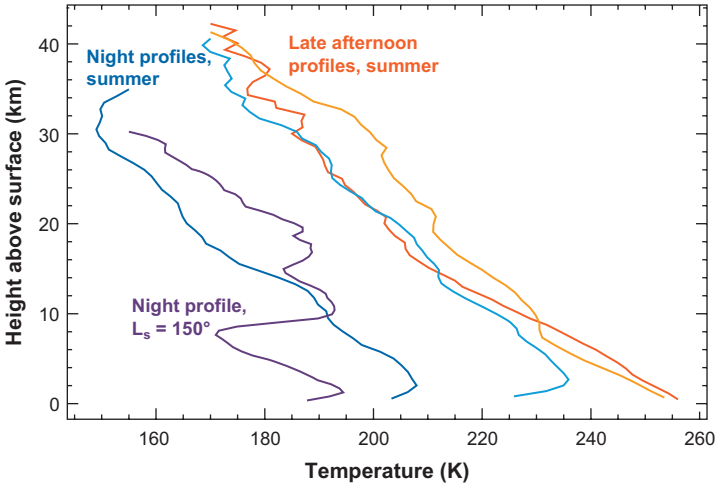

Figure 3

Temperature profiles as a function of height as derived from MGS radio occultation data. Late-afternoon temperatures are shown from southern mid-latitudes during summer. Nighttime temperatures are also shown from mid-latitudes during summer. A nighttime profile is shown with large waves taken near the Tharsis volcanoes at $L_s = 150°$.

resolution of the radio occultation temperature profiles allows characterization of a near-surface inversion layer, which is not apparent in TES profiles. A few radio occultation profiles show large-amplitude waves (purple profile), which may be caused by the presence of water ice clouds (Hinson & Wilson 2004).

Stellar occultation, where a spacecraft watches as a star disappears or reappears from behind the limb of Mars, has been used to retrieve middle-atmospheric (50–130 km) temperatures using UV observations made by the *Mars Express* SPICAM instrument (Quémerais et al. 2006). These observations are important because of the paucity of data at these higher altitudes.

2.2.3. Entry profiles and aerobraking. Five different spacecraft have successfully landed on the surface of Mars. Each carried accelerometers, which measured atmospheric drag during descent through the atmosphere. These measurements, along with the known aerodynamic properties of the spacecraft, allow the density, and thus temperature as a function of height to be inferred. The five profiles from *Viking Landers 1* and *2* (Seiff & Kirk 1977), *Pathfinder* (Magalhães et al. 1999), and MERs *Spirit* and *Opportunity* (Withers & Smith 2006) all have large-amplitude oscillations that grow with height (except perhaps for *Spirit*), which is characteristic of vertically propagating waves.

The practice of aerobraking, or dipping a spacecraft's periapsis into the uppermost part of the atmosphere (typically above 120 km altitude) to induce drag to circularize an orbit, produces an indirect measurement of atmospheric density near aerobraking altitude. This information can be used to estimate temperatures above 120 km altitude in the Martian thermosphere (Keating et al. 1998).

2.2.4. Boundary layer. Observations of atmospheric temperatures from orbit give a very useful large-scale view of the global thermal structure, but even the radio occultation observations do not have sufficient vertical resolution to characterize the details of the near-surface planetary boundary layer (PBL). The PBL is important because it is the portion of the atmosphere that directly interacts with the surface, responding to forcings such as frictional drag and surface heating. PBL temperatures have been measured directly using thermocouples mounted on the *Viking* (Hess et al. 1977) and *Pathfinder* (Schofield et al. 1997) landers, and have been retrieved from thermal infrared spectra taken by the MER Mini-TES instrument (Smith et al. 2006, Spanovich et al. 2006).

Both the thermocouple measurements and the retrieved temperatures using thermal infrared spectra show a consistent diurnal pattern (**Figure 4**). The atmosphere is coolest and stably stratified before dawn. Soon after sunrise, the warming surface heats the atmosphere from the bottom upward. A very steep, superadiabatic vertical temperature gradient is established through the lowest 100 m of the atmosphere by mid-morning. Turbulent convection sets in throughout this lowest layer, with temperature fluctuations of 15 to 20 K recorded in the lowest meter above the surface and up to 5 K in the lowest 100 m on timescales of 30–60 s. Turbulent convection continues until late afternoon (around 16:30), when the cooling surface becomes cooler than the near-surface atmosphere, convection shuts off, and the near-surface

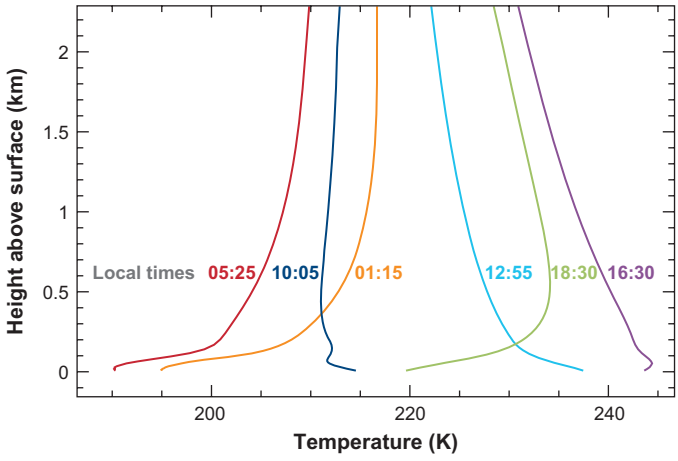

Figure 4

Atmospheric temperatures as a function of height for different times of day derived from upward-looking observations taken by the Mini-TES instrument onboard the *Spirit* MER rover.

temperature gradient becomes inverted. The inversion layer grows throughout the nighttime hours, reaching a depth of at least 1 km before rapidly reversing again in the morning.

2.3. Wind

There are relatively few direct measurements of wind on Mars. The *Viking Landers* (Hess et al. 1977) and *Mars Pathfinder* (Schofield et al. 1997) carried hot-wire anemometers that measured both wind speed and direction. The *Mars Pathfinder* also carried a set of three wind socks mounted at different heights on a mast to measure wind direction (Sullivan et al. 2000). These observations show typical near-surface wind speeds to range from 0–10 m s^{-1}, with a daily rotation of the wind direction vector responding to the combination of downhill drainage flow and the passage of the solar thermal tide. Wind speeds were generally light during the night, with maximum values during the morning. Occasional gusts were also recorded with higher wind speeds.

Wind velocity has been estimated indirectly using the orientation and movement of distinct clouds (Kahn 1984) and the orientation of surface aeolian features. However, wind information from clouds is severely limited both by the sporadic appearance of clouds and by the uncertainty of cloud heights. The link between winds and the morphology of aeolian features is not completely understood and may only reflect the winds during certain seasons or even past climates. A better indirect estimate of wind speeds is obtained using gradient balance, which relates latitudinal gradients in the thermal structure to vertical gradients in zonal wind speed by assuming a balance between horizontal pressure gradient force, the Coriolis force, and centrifugal forces. The drawback to the gradient wind method is that it requires a boundary condition on the zonal wind speed, which is generally taken as zero at the surface.

Figure 5 shows the zonal gradient wind computed from the thermal structure shown in **Figure 2**. In solstice conditions, the steep latitudinal gradient in temperature

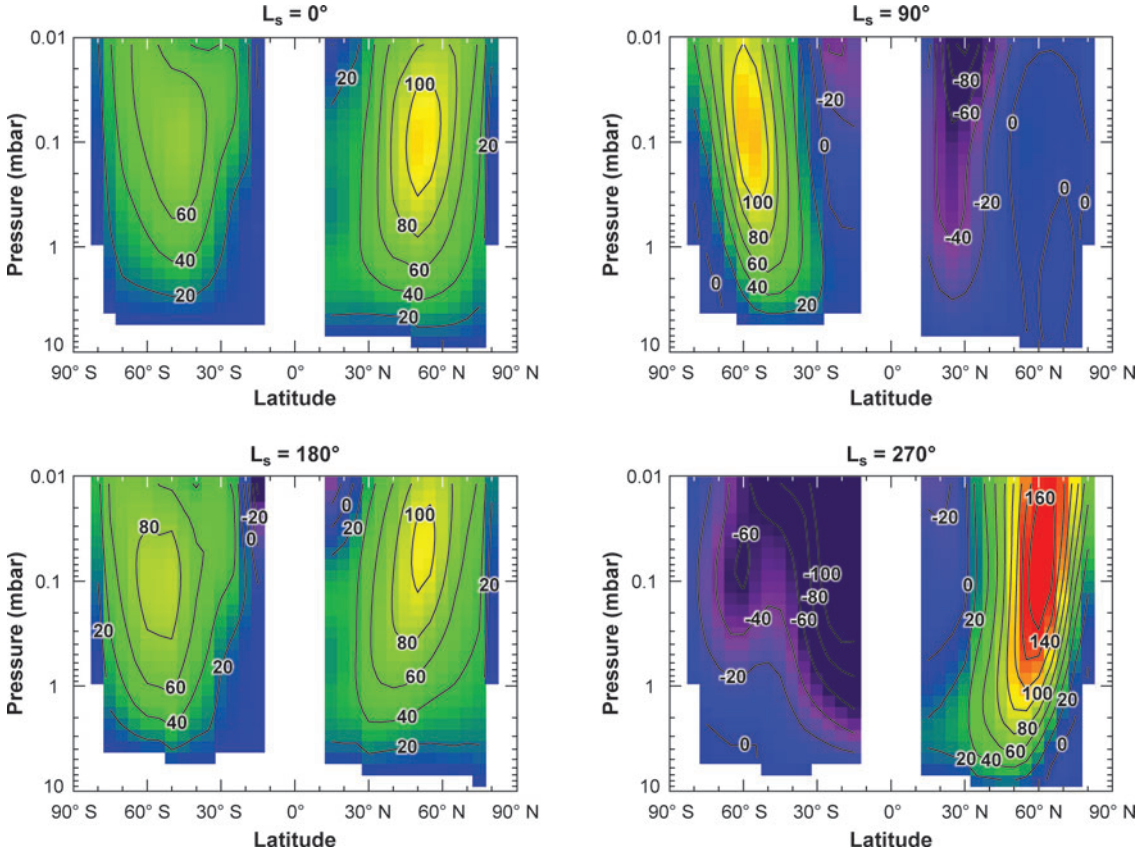

Figure 5

Mean daytime (~2:00 PM) local-time zonal wind speed as a function of latitude and pressure (or height above the surface) as observed by TES using the gradient wind approximation. Wind speeds are given in meters per second, with positive values indicating a wind blowing from west to east.

between the warm mid-latitudes and the cold winter polar night gives rise to a strong eastward jet, or polar vortex, which can reach speeds well in excess of 100 m s^{-1}. Winds are generally light and westward in the summer hemisphere. The polar vortex that forms during the Northern Hemisphere winter ($L_s = 270°$) is noticeably stronger than the Southern Hemisphere winter polar vortex. The thermal structure at solstice is indicative of a single, strong cross-equatorial meridional (Hadley) circulation, with upward motion in the summer hemisphere, cross-equatorial meridional winds from the summer to the winter hemisphere at altitude, downward motion in the winter hemisphere just equatorward of the polar vortex, and return circulation near the surface. In equinox conditions, a moderate mid-latitude eastward jet forms in each hemisphere, with zonal winds in the north being somewhat greater than those in the south. A pair of Hadley cells dominates the meridional

circulation, with upward motion near the equator, poleward flow at altitude, downward motion at mid-latitudes, and a return equatorward flow near the surface in each hemisphere.

2.4. Dust Aerosol

Dust aerosols are always present in the Martian atmosphere. Their presence significantly affects the thermal structure of the atmosphere and is a major driver of atmospheric circulations at all spatial scales.

2.4.1. Dust aerosol optical depth. *Mariner 9* carried the IRIS infrared spectrometer and monitored the decay of the great planet-encircling dust storm of 1971 (Hanel et al. 1972). The IRTM infrared thermal mapper monitored dust optical depth (including two planet-encircling dust storms) during the *Viking* mission (Martin & Richardson 1993). More recently, MGS mapped dust optical depth for three Martian years using thermal infrared spectra from TES (Smith 2004) and daily global imaging from the Mars Orbiter Camera (MOC) (Cantor et al. 2001, Cantor 2007).

At present, data collected by three orbiting spacecraft continue to monitor dust aerosols. The broadband infrared THEMIS instrument on *Mars Odyssey* (Smith et al. 2003) serves as a valuable link between the MGS and the MRO and *Mars Express* observations. On *Mars Express*, the PFS (Grassi et al. 2005b, Zasova et al. 2005), OMEGA, and SPICAM (Montmessin et al. 2006, Rannou et al. 2006) instruments are capable of observing dust optical depth, whereas on MRO, the MCS, CRISM, and MARCI instruments monitor dust.

Observations of the Sun from the surface of Mars by the *Viking Landers* gave dust optical depth at the two lander sites (Colburn et al. 1989), and a similar technique was used by the *Pathfinder* lander (Smith & Lemmon 1999). Currently, the two MERs are monitoring dust optical depth by direct imaging of the Sun by the Pancam instrument (Lemmon et al. 2004) and through retrievals using infrared spectra taken by the Mini-TES instrument (Smith et al. 2006).

The data collected by all these instruments has provided a good overview of the main features of the dust cycle in the current Martian climate. The orbiter observations show a definite seasonal pattern to the occurrence of dust storms and the background level of dust optical depth. The main feature of the annual cycle is the intermittent occurrence of regional- or planetary-scale dust storms. The largest dust storms occur almost exclusively during the dusty season between $L_s = 180°–360°$, when overall surface and atmospheric temperatures are warmest. These events can occasionally grow to become planet-encircling, with dust optical depths exceeding unity over much of the planet. The last two such planet-encircling dust storms erupted in 2001 and 2007 (Smith et al. 2002, Cantor 2007), and it can take a couple months for the dust to settle out back to a nominal level (Conrath 1975). **Figure 6** shows visible-wavelength images of Mars taken by the MGS MOC just before and near the height of the 2001 planet-encircling dust storm (Cantor 2007). Planet-encircling dust storms do not happen every Martian year, but at random intervals that average about once every three Martian years. Regional-scale dust storms do occur every Martian year

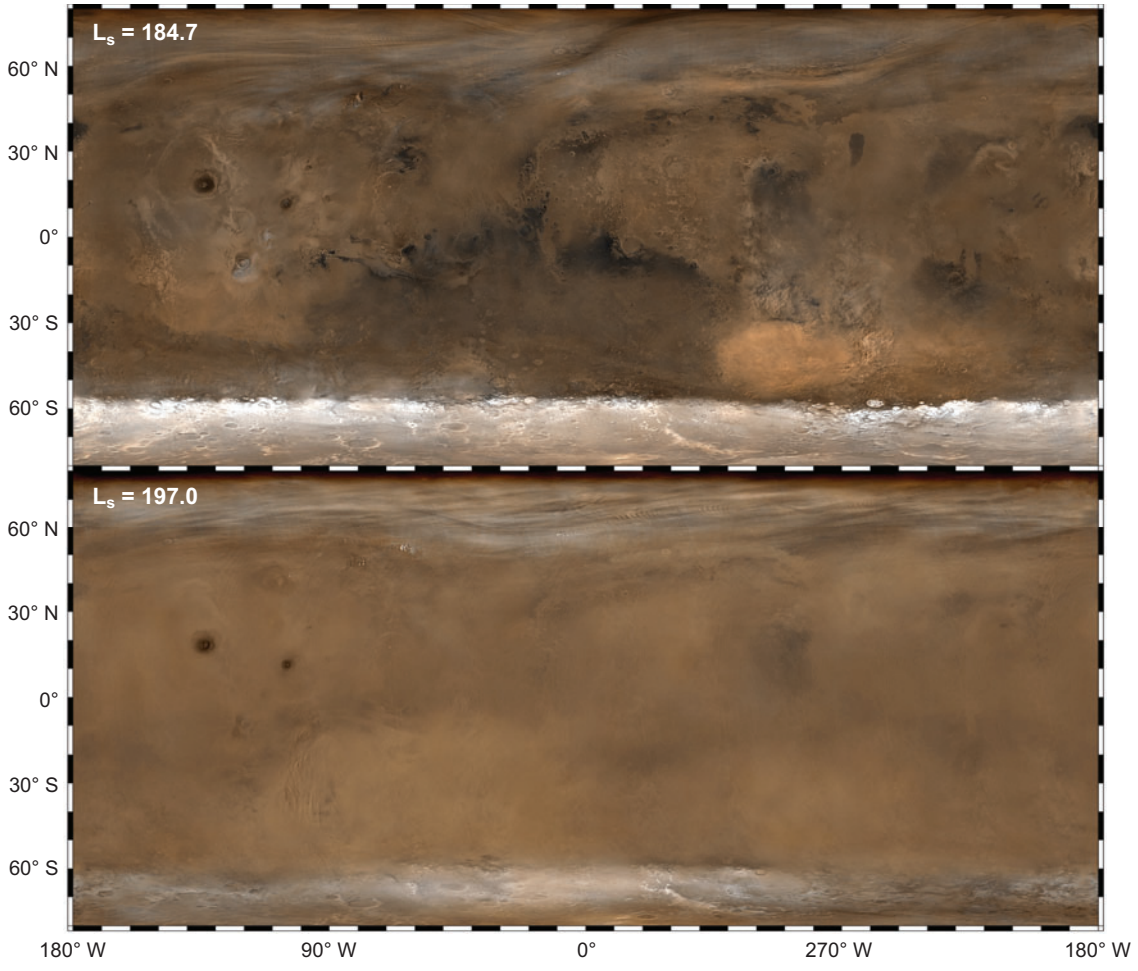

Figure 6

Composites of images taken by the MGS Mars Orbiter Camera over the course of one day. The top images were taken just before the planet-encircling dust storm event of 2001, whereas the bottom images were taken at the height of the dust event.

during the dusty season, particularly near $L_s = 225°$ and 315°, when cross-equatorial flushing dust storms occur (Cantor et al. 2001, Liu et al. 2003, Cantor 2007). These storms typically last a few weeks. Smaller, local-scale dust storms happen throughout the year, and many are associated with either topographic features, such as Valles Marineris, or especially the retreating edge of the seasonal polar ice cap during the spring in both hemispheres (Cantor et al. 2001). The opposite, clear season (L_s = 0°–180°) is characterized by a much lower background level of dust optical depth and no very large dust storms. During this period, local dust storm activity is confined largely to the region near the edge of the seasonal polar ice caps, especially along the

retreating north cap during northern spring, and along the southern cap at the end of southern winter.

2.4.2. Dust aerosol physical properties. Information about the size and shape of dust aerosols is most easily obtained by examining the scattering of light by dust and the amount of absorption by dust at widely separated wavelengths (for example, thermal infrared versus visible optical depth). Following the pioneering work of Hansen & Travis (1974), the aerosol particle size distribution function, $n(r)$, is often expressed in terms of the first two moments of the distribution; the mean or effective radius, r_{eff}; and the dimensionless variance, v_{eff}, as weighted by the geometrical cross section of the particles. Hansen & Travis (1974) demonstrate that the exact form of the underlying size distribution, $n(r)$, is not important for most problems as long as r_{eff} and v_{eff} are specified.

A comprehensive review of determinations of r_{eff} and v_{eff} from ground-based and spacecraft observations for Martian dust is given by Dlugach et al. (2003). Results have been fairly consistent between a variety of different instruments using a number of different techniques. Imaging visible-wavelength sky brightness from the Martian surface as a function of angular distance from the Sun using the *Viking Lander*, *Pathfinder*, and MER cameras is an especially effective way to determine particle size. Estimates from *Viking* (Pollack et al. 1995), *Pathfinder* (Tomasko et al. 1999), and MER (Lemmon et al. 2004) are all within the range $r_{eff} = 1.5$–1.65 μm, $v_{eff} = 0.2$–0.3. Analysis of TES thermal infrared spectra taken as emission-phase functions (EPF), where a fixed spot of the surface is viewed at a wide range of emission angles as an orbiting spacecraft passes over the spot, has been used by Wolff & Clancy (2003) to find an average value of $r_{eff} = 1.5$–1.6 μm, consistent with lander results. Although dust particle size appears to be relatively constant under most conditions, Wolff & Clancy (2003) and Clancy et al. (2003) report smaller dust particles ($r_{eff} \sim 1$ μm) in the Northern Hemisphere during $L_s = 50°$–$200°$, and larger dust particles ($r_{eff} = 1.8$–2.5 μm) during the peak of the 2001 planet-encircling dust storm event. Recent retrievals of r_{eff} using thermal infrared spectra from the MER Mini-TES also show small variations in r_{eff} with season (Wolff et al. 2006). Finally, the comparison of dust optical depth between wavelengths of 9 and 20 microns (e.g., Wolff & Clancy 2003 for TES observations), or between infrared (9 microns) and visible wavelengths (e.g., Clancy et al. 2003 for TES observations; Lemmon et al. 2004, Wolff et al. 2006 for MER observations), give useful constraints on particle size, which have been found to be consistent with the other techniques described above.

It is difficult to obtain much useful information on the shape of dust particles, particularly because their composition is not well known. The best hope for useful constraints is with near-infrared or visible wavelength observations that sample the scattering phase functions using EPFs (from an orbiter) or surveys of sky brightness (from a surface platform). In the thermal infrared, there is little sensitivity to particle shape. Analysis of visible-wavelength TES EPFs by Clancy et al. (2003) indicate that dust is modeled better by disk particle shapes with moderate axial ratios (0.5–2.0) rather than simple spheres.

An identification of the composition of dust aerosols was initially of interest primarily as an analog so that the real and imaginary indices of refraction (and thus scattering properties) could be computed as a function of wavelength. The minerals montmorillonite (Toon et al. 1977) and palagonite (Clancy et al. 1995) were typical early choices based on the similarity of the computed spectral dependence of absorption to that observed in *Mariner 9* IRIS thermal infrared spectra. Later efforts (Snook et al. 2000, using *Mariner 9* IRIS; Wolff & Clancy 2003, using TES) attempted to directly solve for the dust's indices of refraction without identification of a specific composition, the goal being to more accurately retrieve dust optical depth and particle sizes rather than composition information. Bandfield & Smith (2003) and Hamilton et al. (2005) specifically attempted modeling of dust aerosol composition by matching the shape of the observed spectral features against those expected from large libraries of mineral spectra. Bandfield & Smith (2003) found a composition dominated by silicates with both primary and secondary minerals. Hamilton et al. (2005) found that the dust is dominated by framework silicates (probably feldspar), and that dust is largely the product of mechanical weathering of basaltic rocks with minor chemical alteration.

2.4.3. Dust aerosol vertical distribution. The vertical distribution of dust aerosols plays a large role in the vertical distribution of solar energy in the atmosphere. A number of observations have indicated that the simplifying assumption used in many retrieval algorithms (Smith et al. 2003, Smith 2004), that dust is well-mixed with the CO_2 gas, is often good. Analysis of limb scans from the *Viking Lander* Sun diodes (Pollack et al. 1977), images from the *Pathfinder* cameras (Smith et al. 1997), and observations of the Sun near the horizon using the MER Pancam instruments (Lemmon et al. 2004) indicate a scale height for dust consistent with that of the background CO_2 atmosphere. Furthermore, in many cases, TES dust optical depth scales closely with both surface pressure and 1/cos (emission angle), indicating that dust optical depth is proportional to the amount of gas along the line of sight, as expected for well-mixed dust.

However, it is also clear that although the well-mixed approximation might be useful for general-purpose retrievals, the actual vertical distribution of dust is generally different. Images from orbit of the Martian limb by *Mariner 9* (Anderson & Leovy 1978), *Viking* (Jaquin et al. 1986), and MGS MOC (Cantor 2007) show that the haze associated with dust extends much higher above the surface during dust storms than when the atmosphere is less dusty. In images taken during large dust storms, dust has been observed to extend to roughly 60 km above the surface, whereas during nondusty conditions, the maximum height of dust is only 10–20 km.

Observations of dust at the limb in a solar occultation geometry made by Phobos (Chassefière et al. 1992) and the *Mars Express* SPICAM instruments (Montmessin et al. 2006, Rannou et al. 2006) also give good information on the vertical distribution of dust. These observations show detached layers of water ice clouds superimposed on the background dust haze layer. The depth of this haze layer shows dust extending high in the atmosphere during dusty times and confined near the surface near the poles and during the clear season.

2.5. Condensate Clouds

In addition to dust, aerosols in the form of condensate clouds occur frequently on Mars. Condensate clouds made up of water ice and CO_2 ice have been observed.

2.5.1. Water ice cloud optical depth. Water ice clouds play an important part in the water cycle by altering the global transport of water vapor (Clancy et al. 1996). The location of clouds is often indicative of regions of upward-moving air, and serves as a sensitive validation of GCM models (Liu et al. 2003). Water ice aerosols nucleating on dust particles also appear to cleanse the atmosphere of dust and to deposit water ice and dust to the surface in the polar regions (Pearl et al. 2001). Water ice clouds are observed to take on many forms including topographically induced clouds, ground fogs, vast polar hoods, and a low-latitude belt of clouds that forms during the aphelion season between $L_s = 40°$–$140°$ (Anderson & Leovy 1978, Kahn 1984, Clancy et al. 1996, Pearl et al. 2001).

The instruments and retrieval techniques used to identify and determine optical depth for water ice aerosols are much the same as they are for dust. The first determination of water ice cloud optical depth using spacecraft data from Mars was made using *Mariner 9* IRIS thermal infrared spectra (Curran et al. 1973). *Viking*-era clouds were mapped by the IRTM instrument (Tamppari et al. 2000) and imaged by the cameras on the orbiters (Kahn 1984). Much of our current understanding of the seasonal and latitudinal distribution of water ice clouds comes from the MGS observations made over three Martian years by TES (Pearl et al. 2001, Smith 2004) and MOC (Wang & Ingersoll 2002; Benson et al. 2003, 2006). The *Mars Odyssey* THEMIS instrument continues to monitor water ice optical depth (Smith et al. 2003), as do the *Mars Express* PFS, OMEGA, and SPICAM instruments, and the MRO MCS, CRISM, and MARCI instruments. From the surface, clouds have been imaged by the *Viking Landers*, *Pathfinder*, and MERs, providing additional information on their occurrence and morphology.

The optical depth of water ice clouds is often anticorrelated with that of dust. Whereas large dust storms form preferentially during the dusty, perihelion season ($L_s = 180°$–$360°$), the greatest extent of water ice clouds are observed during the cooler aphelion season ($L_s = 0°$–$180°$) and in the polar regions in the winter hemisphere (Tamppari et al. 2000, Pearl et al. 2001, Liu et al. 2003, Smith 2004). Perhaps the most striking cloud feature observed is the appearance during the aphelion season of a low-latitude belt of clouds, which appears to repeat every year with very similar amplitude and spatial distribution. The cloud belt begins to form around $L_s = 0°$, building to maximum intensity and spatial coverage by about $L_s = 80°$. The cloud belt has significant optical depth between 10°S and 30°N latitude, with higher optical depth over topographic highs, such as the Tharsis volcanoes, Olympus Mons, and Elysium, and over the Lunae Planum region to the north of the Valles Marineris. At $L_s = 140°$, the cloud belt quickly disappears as atmospheric temperatures rise, although clouds over the volcanoes remain for much of the year (Benson et al. 2006). The other major cloud features are the polar hoods that form over the polar regions in the winter hemisphere. The northern polar hood is much more extensive than the

southern polar hood, reaching down to nearly 30°N latitude at its greatest extent. There is some indication that polar hood optical depths are highest near the edges of the hood and decrease toward the pole (Liu et al. 2003), which could be caused by an inability of water vapor to penetrate the polar vortex to near the pole (Richardson et al. 2002).

The *Viking Lander* cameras observed both polar hood clouds as well as near-surface water ice ground fogs (Pollack et al. 1977). The *Pathfinder* lander observed water ice clouds near sunrise and sunset (Smith et al. 1997). Repeated imaging of the sky by MER shows that clouds are common at the *Opportunity* site between $L_s = 20°–140°$, and often have a morphology similar to terrestrial cirrus clouds.

Because water ice clouds form by condensation, relatively small changes in atmospheric temperature can cause clouds to form or sublimate quickly, and there can be large changes in water ice cloud optical depth over the course of a day. Although there is not a systematic understanding yet of how cloud optical depths vary throughout the day, there is now considerable evidence that changes in cloud optical depth do occur. Using *Viking Orbiter* IRTM data, Christensen (1998) found that water ice clouds evolved from dispersed hazes to more localized hazes during the day. Further analysis of the IRTM data by Tamppari et al. (2003) found water ice cloud optical depth to be minimum at midday with higher optical depth both in the morning and late afternoon. By comparing the spatial patterns of MGS Mars Orbiter Laser Altimeter (MOLA) absorptions with the differences between observed and modeled nighttime surface temperatures, Wilson et al. (2007) concluded that nighttime water ice cloud optical depths are considerably higher than daytime values in the aphelion season low-latitude cloud belt. Hinson & Wilson (2004) came to a similar conclusion, finding evidence for strong diurnal variations in clouds in the tropics from the waves and thermal structure observed in MGS radio occultation observations. And finally, Smith et al. (2003) found that *Mars Odyssey* THEMIS retrievals of water ice cloud optical depth taken at ∼5:00 PM had higher values than retrievals from contemporaneous observations made by TES at ∼2:00 PM.

2.5.2. Water ice physical properties. As is the case for dust, information about the size and shape of water ice aerosols is most easily obtained by examining scattering as a function of solar phase angle and by comparing the amount of absorption at widely spaced wavelengths. Unlike dust, however, the composition of water ice aerosols is known, which simplifies the analysis somewhat. Modeling of the spectral dependence of water ice absorption in *Mariner 9* IRIS spectra by Curran et al. (1973) led to an estimate of $r_{eff} = 2\ \mu$m. A similar analysis using TES spectra by Pearl et al. (2001) also gave $r_{eff} = 2\ \mu$m, as did near infrared observations made by the Phobos spacecraft (Rodin et al. 1997).

A more comprehensive analysis of the TES data using EPF observations has shown that there are two distinct populations of water ice aerosol (Clancy et al. 2003). Type I water ice aerosols are small ($r_{eff} = 1–2\ \mu$m) and typically appear in high-altitude hazes and in the polar hoods. Type II water ice aerosols are larger ($r_{eff} = 3–4\ \mu$m) and appear most prominently in the aphelion season low-latitude cloud belt. The scattering phase function gives an indication of the shapes of the ice aerosols, but

there are still uncertainties. Type I water ice aerosols have a scattering behavior suggestive of crystalline shapes, which could be the octahedral shape expected for Ice 1c. On the other hand, the larger type II water ice aerosols appear to be more consistent with nonangular, spheroidal shapes (Clancy et al. 2003).

2.5.3. Water ice cloud vertical distribution. The vertical distribution of water ice aerosol is largely controlled by the saturation conditions of the atmosphere and so is sensitive to the abundance of water vapor, and especially to atmospheric temperature as a function of height. Clouds are expected to form at the altitude where atmospheric temperatures become cool enough for water vapor to condense, which varies widely as a function of season and latitude from near the surface to more than 50 km (Smith 2002). Condensation levels are high (>30 km) during the warm perihelion season, but significantly lower (10–20 km) during the cooler aphelion season. Very low condensation levels are found near the winter poles in both hemispheres. Direct observation of water ice cloud heights has been made by imaging at the limb (Anderson & Leovy 1978, Jaquin et al. 1986), estimation of where clouds intersect surface topography (Benson et al. 2003), thermal infrared spectrometer observations by TES at the limb (Pearl et al. 2001), and UV stellar occultation observations by *Mars Express* SPICAM (Rannou et al. 2006). These observations largely confirm the idea that clouds form at the water condensation level, whereas individual discrete clouds are sometimes observed at additional higher altitudes.

2.5.4. CO_2 ice clouds. Evidence for CO_2 ice clouds dates to the early observations made by *Mariner 6* and 7 (Herr & Pimental 1970). The presence of CO_2 ice clouds has been inferred at places where atmospheric temperatures are cold enough for CO_2 to condense (e.g., Schofield et al. 1997, Pearl et al. 2001). The MGS Mars Orbiter Laser Altimeter (MOLA) instrument made systematic observations of CO_2 clouds by observing reflection returns during the polar night in the winter hemisphere that were kilometers above the altitude of the known surface (Neumann et al. 2002). These observations showed that CO_2 ice clouds are common throughout the region of polar winter total darkness.

Clouds have also been detected at very high altitudes (60–100 km above the surface), which implies that they are composed of CO_2 ice aerosols given atmospheric temperatures at that height. The *Pathfinder* lander observed such clouds at very high altitudes in the predawn sky (Smith et al. 1997). Clancy et al. (2007) documented the occurrence of these "Mars equatorial mesospheric clouds" using images from MOC and the TES visible channel bolometer, finding that they most commonly appeared between $L_s = 30°$ and 150° near the equator in two longitude bands (50°–120°W and 320°–360°W) with cloud heights of 60–80 km. Similar clouds have also been observed by the *Mars Odyssey* THEMIS instrument using parallax between different visible-wavelength channels (McConnochie et al. 2006) and by the *Mars Express* SPICAM instrument using UV stellar occultations (Montmessin et al. 2006).

2.6. Water Vapor and Other Trace Gases

Although a few retrievals of water vapor abundance were made using data from early missions such as the *Mariner 9* IRIS instrument (Conrath et al. 1973), the first definitive description of seasonal and latitudinal dependence of water vapor was derived from the *Viking Orbiter* Mars Atmospheric Water Detectors (MAWD) (Jakosky & Farmer 1982). Those data showed a global annual average column abundance of approximately 10 precipitable-microns of water vapor, with higher values over the Northern Hemisphere in the summer reaching a maximum of ~75 precipitable-microns near the north pole at $L_s = 120°$. The MAWD experiment operated by observing water vapor absorption bands in the near-infrared at a wavelength of approximately 1.4 microns. Scattering by dust and ice aerosols is important at these wavelengths and must be accurately accounted for to obtain valid water vapor abundance (Fedorova et al. 2004). Additional early spacecraft observations of water vapor were also provided by the *Phobos* (Rosenqvist et al. 1992) and *Pathfinder* (Titov et al. 1999) spacecraft.

The current best description of seasonal and spatial dependence of water vapor comes from thermal infrared spectra taken by TES (Smith 2002, 2004). The water vapor rotational bands observed by TES at a wavelength of approximately 30 microns are much less affected by aerosols than those in the near-infrared, and the long (nearly three Martian years), systematic coverage of TES allows the analysis of variations over timescales up to interannual length. The TES retrievals of water vapor column abundance show a similar seasonal dependence as MAWD, but with somewhat lower overall abundance, and the addition of a relative maximum in Southern Hemisphere water vapor near the summer pole that was likely masked by large dust storms during MAWD observations. The summertime peak in water vapor column abundance is roughly twice as high in the north as in the south.

The annually averaged column abundance of water vapor observed by TES is shown in **Figure 7**. Apparent is an anticorrelation with topography. Low-lying areas

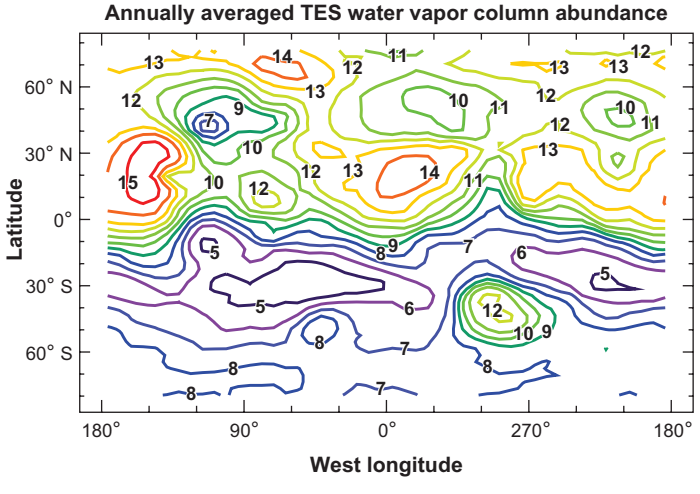

Figure 7

Map showing the spatial distribution of the annually averaged water vapor column abundance (in precipitable microns) as observed by TES.

such as Hellas basin (45°S, 290°W) and almost the entire Northern Hemisphere have higher abundance because there is more atmosphere above those areas. The band of latitudes between roughly 10°S and 40°N has a relatively high annual average because water vapor is maintained there year-round, whereas further north and south there are significant portions of the year with very little water vapor. There is also a significant positive correlation between water vapor abundance and surface albedo (i.e., bright areas have higher water vapor), and a negative correlation with thermal inertia, indicating that surface properties such as pore space size and grain size contribute to how water vapor is distributed.

The seasonal asymmetry in water vapor condensation height allows cross-equatorial Hadley Cell transport of water vapor from south to north during the perihelion season, but inhibits transport from north to south during the aphelion season (Clancy et al. 1996). The result is a more uniform latitudinal distribution of water vapor during the perihelion season, and a steep latitude gradient in water vapor during aphelion, with the formation of a low-latitude water ice cloud belt where water vapor condenses.

Water vapor continues to be an area of great interest in current spacecraft observations. The *Mars Express* has three instruments capable of retrieving water vapor abundance. Like TES, the *Mars Express* PFS instrument observes water vapor in the thermal infrared (Fouchet et al. 2007), whereas the OMEGA (Melchiorri et al. 2007) and SPICAM (Fedorova et al. 2006) instruments observe in the near-infrared. On MRO, both CRISM (near-infrared) and MCS (thermal infrared) are currently monitoring water vapor. The MER Mini-TES instrument can also retrieve column-integrated water vapor from the surface (Smith et al. 2006).

Much of the work characterizing trace gases has been done using ground-based telescopes because the spectral resolution of those instruments is typically much greater than those carried by spacecraft (see Encrenaz 2001 for a review). However, spacecraft observations have also been used to characterize trace gases. The *Viking* mass spectrometer measured the amount of nitrogen and argon, and identified krypton, xenon, and neon (Owen et al. 1977). Maguire (1977) used *Mariner 9* IRIS spectra to place constraints on a number of trace species.

The most commonly studied trace gases (other than water vapor) by spacecraft observations have been carbon monoxide, ozone, and methane. Carbon monoxide has absorption bands in the near-infrared, which have been used by a variety of instruments including *Phobos* ISM (Rosenqvist et al. 1992), *Mars Express* PFS, and OMEGA (Encrenaz et al. 2006), and MRO CRISM to retrieve abundance. Retrievals show an abundance of approximately 700 ppm, with possible variations. Ozone has been observed at UV wavelengths by *Mars Express* SPICAM (Perrier et al. 2006) and MRO MARCI. Ozone is found to show large seasonal and spatial variations that are anti-correlated with water vapor abundance. Observations by MRO CRISM in the near infrared of O_2 singlet delta have also been used as a proxy for ozone because O_2 singlet delta is an excited state of oxygen, which is produced by photodissociation of ozone.

Recently, reports of possible detections of methane in the Mars atmosphere have generated much attention because of the possibility of a biologic origin. Ground-based observations (Krasnopolsky et al. 2004, Mumma et al. 2004) indicate an

abundance of approximately 10 ppb with possible spatial variations, which would be puzzling given the long lifetime (~300 years) of methane on Mars. Most spacecraft instruments currently in orbit lack the spectral resolution and signal-to-noise ratio to detect such a small signal, but Formisano et al. (2004) have claimed a spatially variable detection of methane of 0–30 ppb using *Mars Express* PFS. Clearly, this is a key area to be addressed by future spacecraft with instrumentation specifically designed to measure methane abundance.

3. DISCUSSION

An overview of the seasonal and latitudinal variation of zonally averaged daytime atmospheric temperature at 0.5 mbar (~25 km altitude), dust and water ice aerosol optical depth, and water vapor abundance as observed by MGS TES is shown in **Figure 8**. Shown are nearly three Martian years of observations beginning in March 1999 and ending in August 2004. The current Martian climate has a distinct and generally repeatable dependence on season, latitude, and longitude. In particular, the perihelion season (L_s = 180°–360°) is relatively warm, dusty, and free of water ice clouds. In contrast, the aphelion season (L_s = 0°–180°) is relatively cool, cloudy, and free of dust. Water vapor abundance is largest in both hemispheres near the summer pole. The perihelion season shows a high degree of interannual variability in atmospheric temperature and dust optical depth, primarily associated with the intermittent nature of large dust storm events. The aphelion season shows relatively little interannual variability in temperatures and aerosol optical depth.

3.1. Interannual Variation

The long-term success of several spacecraft, including *Viking*, MGS, *Mars Odyssey*, MER, and *Mars Express*, has resulted in a growing multiyear record of Martian atmospheric conditions, enabling an evaluation of variation from year to year. When comparing observations taken during different years, it is useful to use the "Mars Year" numbering system of Clancy et al. (2000), where 11 April 1955 is adopted as the beginning (L_s = 0°) of Mars Year 1 (MY 1).

The top panel of **Figure 9** shows globally averaged daytime temperatures at a pressure level of 0.5 mbar (approximately 25 km altitude) as a function of season (L_s) as observed by the *Viking* IRTM, MGS TES, and *Mars Odyssey* THEMIS instruments. Globally averaged temperatures follow a well-defined seasonal cycle. The annual minimum occurs near L_s = 40° at a temperature of approximately 165 K (at 0.5 mbar). This is earlier than the time of aphelion (L_s = 71°). Temperatures are usually very repeatable throughout the entire aphelion season, with year-to-year temperature differences within the measurement uncertainties. The perihelion season shows large temperature differences from year to year. These differences, associated with the intermittent occurrence of large dust storms, can be 20 K or larger. Excluding the effect of large dust storms, globally averaged atmospheric temperatures (at 0.5 mbar) peak at around L_s = 260° at approximately 200 K, giving a peak-to-peak annual range of approximately 35 K.

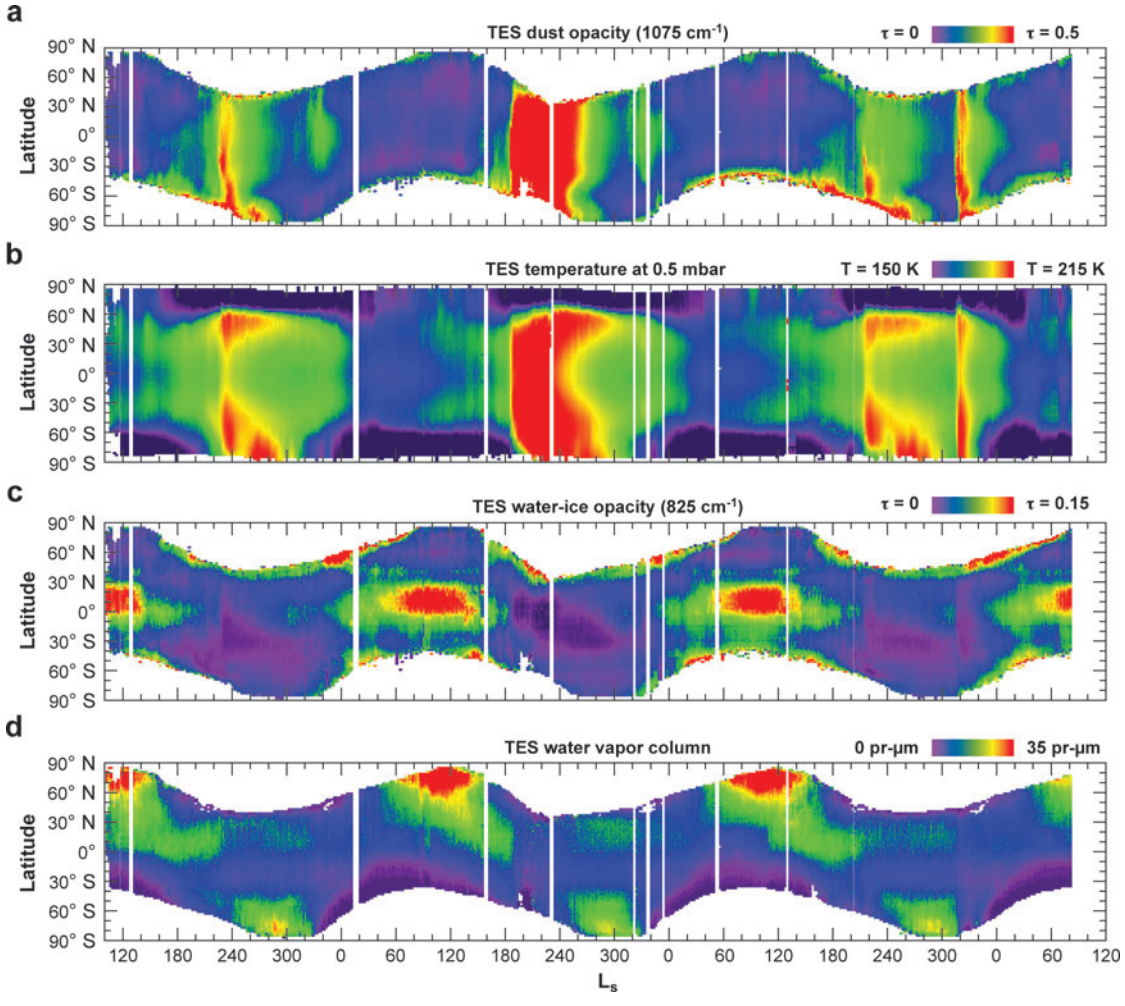

Figure 8

An overview of TES atmospheric daytime observations showing the seasonal and latitudinal variation of (*a*) dust optical depth (at a wavelength of 9 microns), (*b*) atmospheric temperatures (K) at 0.5 mbar (~25 km), (*c*) water ice optical depth (at a wavelength of 12 microns), and (*d*) water vapor column abundance (precipitable microns). Data gaps (*white vertical bands*) were caused by spacecraft anomalies and solar conjunction.

The bottom panel of **Figure 9** shows globally averaged dust optical depth as a function of season for the same spacecraft. The occurrence of the largest dust storms is clearly stochastic, but does show preferred seasons and locations (see also **Figure 8**). The perihelion season appears to have a background 9-micron dust optical depth of approximately 0.15. Superimposed on this level are a number of dust storms, which vary greatly in both intensity and timing. The periods near $L_s = 225°$ and 315° appear particularly favorable for the formation of regional-scale dust storms

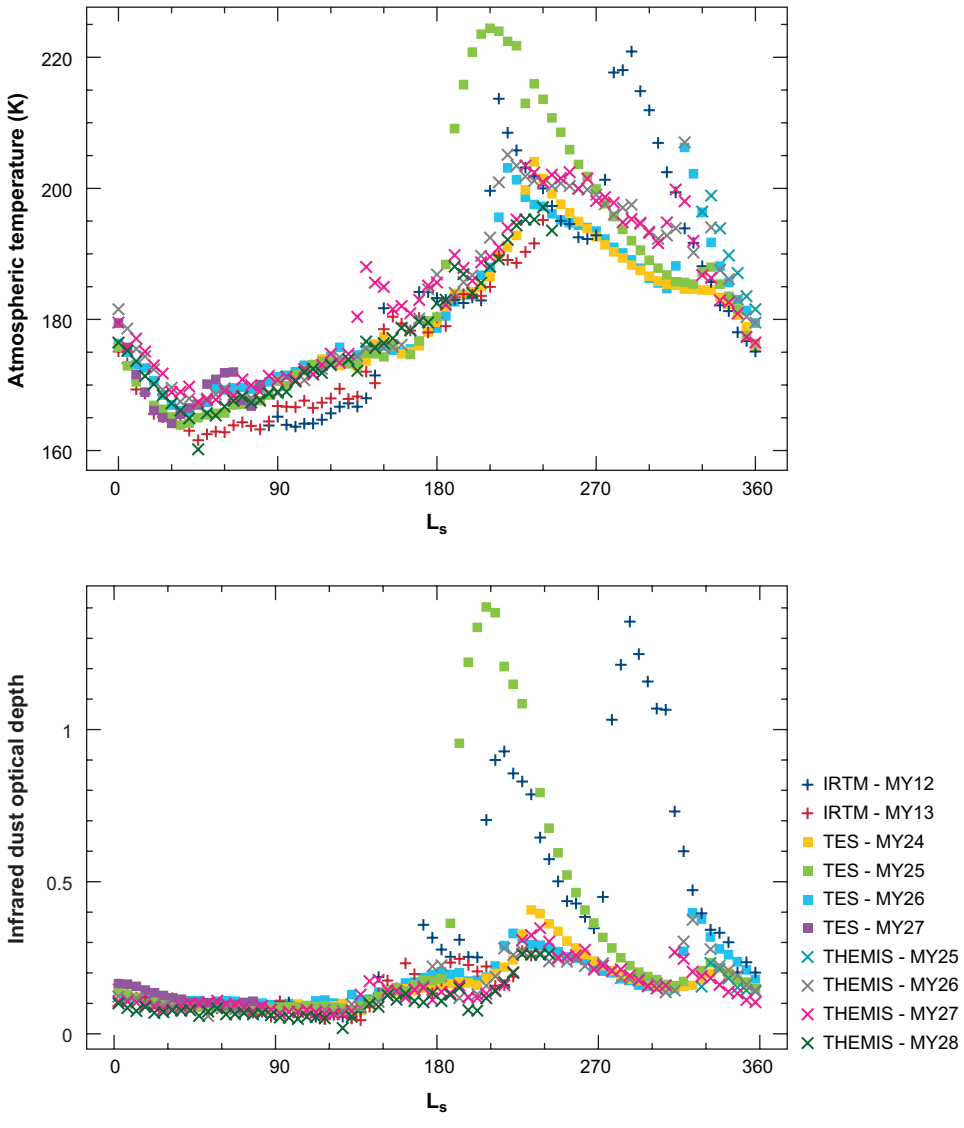

Figure 9

Globally averaged values of (*a*) atmospheric temperatures at ~25 km, and (*b*) infrared dust optical depth as observed by the *Viking* IRTM, MGS TES, and *Mars Odyssey* THEMIS instruments. The aphelion season (L_s = 0°–180°) is relatively cool, free of dust, and shows little variation from year to year, whereas the perihelion season (L_s = 180°–360°) is relatively warm, dusty, and shows large interannual variations caused by dust storms.

(Liu et al. 2003, Smith 2004). After $L_s = 0°$, dust optical depth gradually decays to a minimum level of 0.05 at $L_s = 135°$, after which global dust optical depth begins to rise again. The aphelion season shows much less interannual variability, and no regional- or global-scale dust storms.

Low-latitude water ice optical depth is roughly anticorrelated with dust optical depth, with maximum values in the aphelion season at about $L_s = 110°$ and low values during the perihelion season. The tropical cloud belt that forms during the aphelion season (see **Figure 8**) is remarkably repeatable from year to year, with clouds forming over the same regions with approximately the same optical depth. At high latitudes, polar hood clouds form over the winter polar regions in a similar pattern each year.

The largest interannual variation in water vapor appears to be in the Southern Hemisphere summertime maximum, which may be affected by the variability in temperatures caused by dust storms. The almost complete lack of a Southern Hemisphere summertime maximum in *Viking Orbiter* MAWD observations (Jakosky & Farmer 1982) is likely because the water vapor was masked by two planet-encircling dust storms (Smith 2002, Fedorova et al. 2004), but year-to-year variations of up to ~20% appear to be real.

SUMMARY POINTS

1. A first overall view of the current Martian climate has now been obtained. The climate pattern shows distinct and generally repeatable dependence on season, latitude, and longitude.
2. The perihelion season ($L_s = 180°–360°$) is relatively warm, dusty, and free of water ice clouds, whereas the aphelion season ($L_s = 0°–180°$) is relatively cool, cloudy, and free of dust. Water vapor abundance is largest in both hemispheres near the summer pole.
3. The most prominent "weather" is associated with large dust storm events, which occur stochastically, but in preferred seasons and locations.
4. The greatest interannual variation occurs during the perihelion season and is associated with intermittent large dust storm events. There is low interannual variation during the aphelion season.
5. The seasonal change in the water vapor condensation level leads to asymmetric transport of water vapor from one hemisphere to the other.

FUTURE ISSUES

1. Continued monitoring of the Martian atmosphere is needed to more fully characterize interannual variability in the current Martian climate. Better coverage in local time would be helpful to better characterize wavemodes and diurnal variations of water vapor and water ice clouds.

2. The direct observation of wind velocity as a function of height with global coverage would be an important addition to the characterization of the climate.
3. Characterization of minor gases (especially methane) and isotope ratios is important for understanding the history of the atmosphere.
4. Better characterization of the vertical distribution of aerosols and gases is needed to better model radiative balance and dynamics.
5. Better characterization of the planetary boundary layer using in situ or landed spacecraft is needed to understand the complicated dynamics and important surface-atmosphere interactions in that region.
6. Further modeling of observations can be used to better understand the physical processes behind observed phenomena such as the stochastic nature of dust storms, the seasonal and spatial distribution of water vapor, and the thermal structure of the atmosphere.
7. Sufficient observations are needed to provide useful predictions for the planning of future missions and to support ongoing landed mission operations.

DISCLOSURE STATEMENT

The authors are not aware of any biases that might be perceived as affecting the objectivity of this review.

ACKNOWLEDGMENTS

The author thanks Michael Wolff for his encouragement and help with this review, especially in the section on aerosols. He also thanks Bruce Cantor for images of dust storms from the MGS MOC camera, Paul Withers for temperature profiles obtained by the MER *Spirit* and *Opportunity* rovers during their descent through the atmosphere, and John Wilson for *Viking* IRTM temperatures.

LITERATURE CITED

Anderson E, Leovy C. 1978. Mariner 9 television limb observations of dust and ice hazes on Mars. *J. Atmos. Sci.* 35:723–34

Bandfield JL, Smith MD. 2003. Multiple emission angle surface-atmosphere separations of thermal emission spectrometer data. *Icarus* 161:47–63

Banfield D, Conrath BJ, Smith MD, Christensen PR, Wilson RJ. 2003. Forced waves in the Martian atmosphere from MGS TES nadir data. *Icarus* 161:319–45

Banfield D, Conrath BJ, Gierasch PJ, Wilson RJ, Smith MD. 2004. Traveling waves in the Martian atmosphere from MGS TES nadir data. *Icarus* 170:365–403

Benson JL, Bonev BP, James PB, Shan KJ, Cantor BA, Caplinger MA. 2003. The seasonal behavior of water ice clouds in the Tharsis and Valles Marineris regions of Mars: Mars Orbiter Camera observations. *Icarus* 165:34–52

Benson JL, James PB, Cantor BA, Remigio R. 2006. Interannual variability of water ice clouds over major Martian volcanoes observed by MOC. *Icarus* 184:365–71

Cantor BA. 2007. MOC observations of the 2001 Mars planet-encircling dust storm. *Icarus* 186:60–96

Cantor BA, James PB, Caplinger M, Wolff MJ. 2001. Martian dust storms: 1999 Mars Orbiter Camera observations. *J. Geophys. Res.* 106:23653–87

Chassefière E, Blamont JE, Krasnopolsky VA, Korablev OI, Atreya SK, West RA. 1992. Vertical structure and size distributions of Martian aerosols from solar occultation measurements. *Icarus* 97:46–69

Christensen PR. 1998. Variations in Martian surface composition and cloud occurrence determined from thermal infrared spectroscopy: analysis of Viking and Mariner 9 data. *J. Geophys. Res.* 103:1733–46

Clancy RT, Lee SW, Gladstone GR, McMillan WW, Roush T. 1995. A new model for Mars atmospheric dust based upon analysis of ultraviolet through infrared observations from Mariner 9, Viking, and Phobos. *J. Geophys. Res.* 100:5251–64

Clancy RT, Grossman AW, Wolff MJ, James PB, Rudy DJ, et al. 1996. Water vapor saturation at low altitudes around aphelion: a key to Mars climate? *Icarus* 122:36–62

Clancy RT, Sandor BJ, Wolff MJ, Christensen PR, Smith MD, et al. 2000. An intercomparison of ground-based millimeter, MGS TES, and Viking atmospheric temperature measurements: seasonal and interannual variability of temperatures and dust loading in the global Mars atmosphere. *J. Geophys. Res.* 105:9553–71

Clancy RT, Wolff MJ, Christensen PR. 2003. Mars aerosol studies with the MGS TES emission phase function observations: optical depths, particle sizes, and ice cloud types vs latitude and solar longitude. *J. Geophys. Res.* 108:doi:10.1029/2003JE002058

Clancy RT, Wolff MJ, Whitney BA, Cantor BA, Smith MD. 2007. Mars equatorial mesospheric clouds: global occurrence and physical properties from Mars Global Surveyor Thermal Emission Spectrometer and Mars Orbiter Camera limb observations. *J. Geophys. Res.* 112:doi:10.1029/2006JE002805

Colburn D, Pollack JB, Haberle R. 1989. Diurnal variations in optical depth at Mars. *Icarus* 79:159–89

Conrath BJ. 1972. Vertical resolution of temperature profiles obtained from remote radiation measurements. *J. Atmos. Sci.* 29:1262–71

Conrath BJ. 1975. Thermal structure of the Martian atmosphere during the dissipation of the dust storm of 1971. *Icarus* 24:36–46

Conrath BJ, Curran R, Hanel R, Kunde V, Maguire WC, et al. 1973. Atmospheric and surface properties of Mars obtained by infrared spectroscopy on Mariner 9. *J. Geophys. Res.* 78:4267–78

Conrath BJ, Pearl JC, Smith MD, Maguire WC, Christensen PR, et al. 2000. Mars Global Surveyor Thermal Emission Spectrometer (TES) observations: atmospheric temperatures during aerobraking and science phasing. *J. Geophys. Res.* 105:9509–19

Curran RJ, Conrath BJ, Hanel RA, Kunde VG, Pearl JC. 1973. Mars: Mariner 9 spectroscopic evidence for H_2O ice clouds. *Science* 182:381–83

Dlugach ZM, Korablev OI, Morozhenko AV, Moroz VI, Petrova EV, Rodin AV. 2003. Physical properties of dust in the Martian atmosphere: analysis of contradictions and possible ways of their resolution. *Solar Syst. Res.* 37:1–19

Encrenaz T. 2001. The atmosphere of Mars as constrained by remote sensing. *Space Sci. Rev.* 96:411–24

Encrenaz T, Fouchet T, Melchiorri R, Drossart P, Gondet B, et al. 2006. Seasonal variations of the Martian CO over Hellas as observed by OMEGA/Mars Express. *Astron. Astrophys.* 459:265–70

Fedorova AA, Korablev O, Bertaux J-L, Rodin AV, Kiselev A, Pettier S. 2006. Mars water vapor abundance from SPICAM IR spectrometer: seasonal and geographic distributions. *J. Geophys. Res.* 111:doi:10.1029/2006JE002695

Fedorova AA, Rodin AV, Baklanova IV. 2004. MAWD observations revisited: seasonal behavior of water vapor in the Martian atmosphere. *Icarus* 171:54–67

Formisano V, Atreya S, Encrenaz T, Ignatiev NI, Giuranna M. 2004. Detection of methane in the atmosphere of Mars. *Science* 306:1758–61

Fouchet T, Lellouch E, Ignatiev NI, Forget F, Titov DV, et al. 2007. Martian water vapor: Mars Express PFS/LW observations. *Icarus* 190:32–49

Grassi D, Fiorenza C, Zasova LV, Ignatiev NI, Maturilli A, et al. 2005a. The Martian atmosphere above great volcanoes: early planetary fourier spectrometer observations. *Planet. Space Sci.* 53:1053–64

Grassi D, Ignatiev NI, Zasova LV, Maturilli A, Formisano V, et al. 2005b. Methods for the analysis of data from the Planetary Fourier Spectrometer on the Mars Express mission. *Planet. Space Sci.* 53:1017–34

Hamilton VE, McSween HY Jr, Hapke B. 2005. Mineralogy of Martian atmospheric dust inferred from thermal infrared spectra of aerosols. *J. Geophys. Res.* 110:doi:10.1029/2005JE002501

Hanel RA, Conrath BJ, Hovis WA, Kunde VG, Lowman PD, et al. 1972. Investigation of the Martian environment by infrared spectroscopy on Mariner 9. *Icarus* 17:423–42

Hansen JE, Travis LD. 1974. Light scattering in planetary atmospheres. *Space Sci. Rev.* 16:527–610

Herr K, Pimental G. 1970. Evidence for solid carbon dioxide in the upper atmosphere of Mars. *Science* 167:47–49

Hess SL, Henry RM, Leovy CB, Ryan JA, Tillman JE. 1977. Meteorological results from the surface of Mars: Viking 1 and 2. *J. Geophys. Res.* 82:4559–74

Hinson DP, Simpson RA, Twicken JD, Tyler GL, Flasar FM. 1999. Initial results from radio occultation measurements with Mars Global Surveyor. *J. Geophys. Res.* 104:26997–7012

Hinson DP, Smith MD, Conrath BJ. 2004. Comparison of atmospheric temperatures obtained through infrared sounding and radio occultation by Mars Global Surveyor. *J. Geophys. Res.* 109:doi:10.1029/2004JE002344

Hinson DP, Wilson RJ. 2004. Temperature inversions, thermal tides, and water ice clouds in the Martian tropics. *J. Geophys. Res.* 109:doi:10.1029/2003JE002129

Jakosky BM, Farmer CB. 1982. The seasonal and global behavior of water vapor in the Mars atmosphere: complete global results of the Viking Atmospheric Water Detector Experiment. *J. Geophys. Res.* 87:2999–3019

Jakosky BM, Haberle RM. 1992. The seasonal behavior of water on Mars. See Kieffer et al. 1992, 28:969–1016

James PB, Kieffer HH, Paige DA. 1992. The seasonal cycle of carbon dioxide on Mars. See Kieffer et al. 1992, 27:934–68

Jaquin F, Gierasch PJ, Kahn R. 1986. The vertical structure of limb hazes in the Martian atmosphere. *Icarus* 68:442–61

Kahn RA. 1984. The spatial and seasonal distribution of Martian clouds, and some meteorological implications. *J. Geophys. Res.* 89:6671–88

Kahn RA, Martin TZ, Zurek RW, Lee SW. 1992. The Martian dust cycle. See Kieffer et al. 1992, 29:1017–53

Keating GM, Bougher SW, Zurek RW, Tolson RH, Cancro GJ, et al. 1998. The structure of the upper atmosphere of Mars: in situ accelerometer measurements from Mars Global Surveyor. *Science* 279:1672–76

Kieffer HH, Jakosky BM, Snyder CW, Matthews MS, eds. 1992. *Mars*. Tucson: Univ. Ariz. Press

Krasnopolsky VA, Maillard JP, Owen TC. 2004. Detection of methane in the Martian atmosphere: evidence for life? *Icarus* 172:537–47

Lemmon MT, Wolff MJ, Smith MD, Clancy RT, Banfield D, et al. 2004. Atmospheric imaging results from the Mars Exploration Rovers: Spirit and Opportunity. *Science* 306:1753–56

Leovy CB. 1979. Martian meteorology. *Annu. Rev. Astron. Astrophys.* 17:387–413

Liu J, Richardson MI, Wilson RJ. 2003. An assessment of the global, seasonal, and interannual spacecraft record of Martian climate in the thermal infrared. *J. Geophys. Res.* 108:doi:10.1029/2002JE001921

Magalhães JA, Schofield JT, Seiff A. 1999. Results of the Mars Pathfinder atmospheric structure investigation. *J. Geophys. Res.* 104:8943–56

Maguire WC. 1977. Martian isotope ratios and upper limits for possible minor constituents as derived from Mariner 9 infrared spectrometer data. *Icarus* 32:85–97

Martin TZ, Kieffer HH. 1979. Thermal infrared properties of the Martian atmosphere. 2. The 15-mm band measurements. *J. Geophys. Res.* 84:2843–52

Martin TZ, Richardson MI. 1993. New dust opacity mapping from Viking infrared thermal mapper data. *J. Geophys. Res.* 98:10941–49

McConnochie TH, Bell JF, Savransky D, Wolff MJ, Richardson MI, et al. 2006. *Martian mesospheric clouds: latest results from THEMIS-VIS*. Presented at Fall Meet. Am. Geophys. Union, San Francisco

Melchiorri R, Encrenaz T, Fouchet T, Drossart P, Lellouch E, et al. 2007. Water vapor mapping on Mars using OMEGA/Mars Express. *Planet. Space Sci.* 55:333–42

Montmessin F, Quémerais E, Bertaux JL, Korablev O, Rannou P, Lebonnois S. 2006. Stellar occultations at UV wavelengths by the SPICAM instrument: retrieval and analysis of Martian haze profiles. *J. Geophys. Res.* 111:doi:10.1029/2005JE002662

Mumma MJ, Novak RE, DiSanti MA, Bonev BP, Dello Russo N. 2004. Detection and mapping of methane and water on Mars. *Bull. Am. Astron. Soc.* 36:1127

Neumann GA, Smith DE, Zuber MT. 2002. Two Mars years of clouds detected by the Mars Orbiter Laser Altimeter. *J. Geophys. Res.* 108:doi:10.1029/2002JE001849

Owen T. 1992. The composition and early history of the atmosphere of Mars. See Kieffer et al. 1992, 25:818–34

Owen T, Biemann K, Rushneck DR, Biller JE, Howarth DW, et al. 1977. The composition of the atmosphere at the surface of Mars. *J. Geophys. Res.* 82:4635–39

Pearl JC, Smith MD, Conrath BJ, Bandfield JL, Christensen PR. 2001. Observations of Martian ice clouds by the Mars Global Surveyor Thermal Emission Spectrometer: the first year. *J. Geophys. Res.* 106:12325–38

Perrier S, Bertaux J-L, Lefèvre F, Lebonnois S, Korablev O, et al. 2006. Global distribution of total ozone on Mars from SPICAM/MEX UV measurements. *J. Geophys. Res.* 111:doi:10.1029/2006JE002681

Pollack JB, Colburn D, Kahn R, Hunter J, Van Camp W, et al. 1977. Properties of aerosols in the Martian atmosphere as inferred from Viking lander imaging data. *J. Geophys. Res.* 82:4479–96

Pollack JB, Ockert-Bell ME, Sheppard MK. 1995. Viking lander analysis of Martian atmospheric dust. *J. Geophys. Res.* 100:5235–50

Quémerais E, Bertaux J-L, Korablev O, Dimarellis E, Cot C, et al. 2006. Stellar occultations observed by SPICAM on Mars Express. *J. Geophys. Res.* 111:doi:10.1029/2005JE002604

Rannou P, Perrier S, Bertaux J-L, Montmessin F, Korablev O, Rébérac A. 2006. Dust and cloud detection at the Mars limb with UV scattered sunlight with SPICAM. *J. Geophys. Res.* 111:doi:10.1029/2006JE002693

Richardson MI, Wilson RJ, Rodin AV. 2002. Water ice clouds in the Martian atmosphere: general circulation model experiments with a simple cloud scheme. *J. Geophys. Res.* 107:doi:10.1029/2001JE001804

Rodin AV, Korablev OI, Moroz VI. 1997. Vertical distribution of water in the near-equatorial troposphere of Mars: water vapor and clouds. *Icarus* 125:212–29

Rosenqvist J, Drossart P, Combes M, Encrenaz T, Lellouch E, et al. 1992. Minor constituents in the Martian atmosphere from the ISM/Phobos experiment. *Icarus* 98:254–70

Schofield JT, Barnes JR, Crisp D, Haberle RM, Larsen S, et al. 1997. The Mars Pathfinder Atmospheric Structure Investigation/Meteorology. *Science* 278:1752–57

Seiff A, Kirk DB. 1977. Structure of the atmosphere of Mars in summer at mid-latitudes. *J. Geophys. Res.* 82:4364–78

Smith MD. 2002. The annual cycle of water vapor as observed by the Thermal Emission Spectrometer. *J. Geophys. Res.* 107:doi:10.1029/2001JE001522

Smith MD. 2004. Interannual variability in TES atmospheric observations of Mars during 1999–2003. *Icarus* 167:148–65

Smith MD, Bandfield JL, Christensen PR, Richardson MI. 2003. Thermal Emission Imaging System (THEMIS) infrared observations of atmospheric dust and water ice cloud optical depth. *J. Geophys. Res.* 108:doi:10.1029/2003JE002115

Smith MD, Pearl JC, Conrath BJ, Christensen PR. 2002. Thermal Emission Spectrometer observations of Martian planet-encircling dust storm 2001a. *Icarus* 157:259–63

Smith MD, Wolff MJ, Spanovich N, Ghosh A, Banfield D, et al. 2006. One Martian year of atmospheric observations using MER Mini-TES. *J. Geophys. Res.* 111:doi:10.1029/2006JE002770

Smith PH, Bell JF III, Bridges NT, Britt DT, Gaddis L, et al. 1997. Results from the Mars Pathfinder Camera. *Science* 278:1758–64

Smith PH, Lemmon MT. 1999. Opacity of the Martian atmosphere measured by the imager for Mars Pathfinder. *J. Geophys. Res.* 104:8975–85

Snook KJ, Bandfield JL, Forget F, McKay CP. 2000. Derivation of infrared optical properties of dust suspended in the Martian atmosphere from MGS-TES. *Bull. Am. Astron. Soc.* 32:1094–95

Spanovich N, Smith MD, Smith PH, Wolff MJ, Christensen PR, Squyres SW. 2006. Surface and near-surface atmospheric temperatures from the Mars Exploration Rover landing sites. *Icarus* 180:314–20

Sullivan R, Greeley R, Kraft M, Wilson G, Golombek M. 2000. Results of the imager for Mars Pathfinder windsock experiment. *J. Geophys. Res.* 105:24547–62

Tamppari LK, Zurek RW, Paige DA. 2000. Viking-era water-ice clouds. *J. Geophys. Res.* 105:4087–107

Tamppari LK, Zurek RW, Paige DA. 2003. Viking-era diurnal water-ice clouds. *J. Geophys. Res.* 108:doi:10.1029/2002JE001911

Tillman JE, Johnson NC, Guttorp P, Percival DB. 1993. The Martian annual atmospheric pressure cycle—years without great dust storms. *J. Geophys. Res.* 98:10963–71

Titov DV, Markiewicz MJ, Thomas N, Keller HU, Sablotny RM, et al. 1999. Measurements of the atmospheric water vapor on Mars by the imager for Mars Pathfinder. *J. Geophys. Res.* 104:9019–26

Tomasko MG, Doose LR, Lemmon MT, Wegryn E, Smith PH. 1999. Properties of dust in the Martian atmosphere from the imager on Mars Pathfinder. *J. Geophys. Res.* 104:8987–9008

Toon OB, Pollack JB, Sagan C. 1977. Physical properties of the particles composing the Martian dust storm of 1971–1972. *Icarus* 30:663–96

Wang H, Ingersoll AP. 2002. Martian clouds observed by Mars Global Surveyor Mars Orbiter Camera. *J. Geophys. Res.* 107:doi:10.1029/2001JE001815

Wilson RJ, Richardson MI. 2000. The Martian atmosphere during the Viking mission, I: Infrared measurements of atmospheric temperature revisited. *Icarus* 145:555–79

Wilson RJ, Neumann GA, Smith MD. 2007. Diurnal variation and radiative influence of Martian water ice clouds. *Geophys. Res. Let.* 34:doi:10.1029/2006GL027976

Withers P, Smith MD. 2006. Atmospheric entry profiles from the Mars Exploration Rovers Spirit and Opportunity. *Icarus* 185:133–42

Wolff MJ, Clancy RT. 2003. Constraints on the size of Martian aerosols from Thermal Emission Spectrometer observations. *J. Geophys. Res.* 108:doi:10.1029/2003JE002057

Wolff MJ, Smith MD, Clancy RT, Spanovich N, Whitney BA, et al. 2006. Constraints on dust aerosols from the Mars exploration rovers using MGS overflights and Mini-TES. *J. Geophys. Res.* 111:doi:10.1029/2006JE002786

Zasova L, Formisano V, Moroz V, Grassi D, Ignatiev N, et al. 2005. Water clouds and dust aerosols observations with PFS MEX at Mars. *Planet. Space Sci.* 53:1065–77

Zurek RW. 1981. Inference of dust opacities for the 1977 Martian great dust storms from Viking Lander 1 pressure data. *Icarus* 45:202–15

Zurek RW, Barnes JR, Haberle RM, Pollack JB, Tillman JE, Leovy CB. 1992. Dynamics of the atmosphere of Mars. See Kieffer et al. 1992, 26:835–933

Annual Review
of Earth and
Planetary Sciences
Volume 36, 2008

Contents

Indexes

Errata

An online log of corrections to *Annual Review of Earth and Planetary Sciences* articles may be found at http://earth.annualreviews.org